

Towards Architecture-Agnostic Untrained Network Priors for Image Reconstruction with Frequency Regularization

Yilin Liu¹, Yunkui Pang¹, Jiang Li¹, Yong Chen², and Pew-Thian Yap¹

¹ UNC Chapel Hill

² Case Western Reserve University

Abstract. Untrained networks inspired by deep image prior have shown promising capabilities in recovering a high-quality image from noisy or partial measurements, without requiring training data. Their success has been widely attributed to the spectral bias acting as an implicit regularization induced by suitable network architectures. However, applications of such network-based priors often entail superfluous architectural decisions, overfitting risks, and slow optimization, all of which hinder their practicality. In this work, we propose efficient, architecture-agnostic methods for a more direct frequency control over the network priors: 1) constraining the bandwidth of the white-noise input, 2) controlling the bandwidth of the interpolation-based upsamplers, and 3) regularizing the Lipschitz constants of the layers. We show that even with *just one extra line of code*, the overfitting issues in underperforming architectures can be alleviated such that their performance gaps with the high-performing counterparts can be largely closed despite their distinct configurations, mitigating the need for architecture tuning. This then makes it possible to employ a more *compact* model to achieve similar or superior performance to larger models with greater efficiency. Our regularized network priors compare favorably with current supervised and self-supervised methods on MRI reconstruction and image inpainting tasks, serving as a stronger zero-shot baseline reconstructor. Our code will be made publicly available.

1 Introduction

Magnetic resonance imaging (MRI) is a mainstream imaging tool for medical diagnosis. Reconstructing MR images from raw measurements refers to the transformation from Fourier spectrum of the object in k -space to image space. Since acquiring full k -space measurements is time-consuming, under-sampled k -space data are often collected to reduce scan times. Accelerated MRI is thus known as an ill-posed inverse problem that conventionally requires handcrafted priors [27, 31] to mitigate the resulting aliasing artifacts in the output images. While supervised learning methods based on convolutional neural networks (CNNs) have demonstrated better reconstruction quality with fewer measurements, their training relies on paired under-sampled and fully-sampled measurements, which

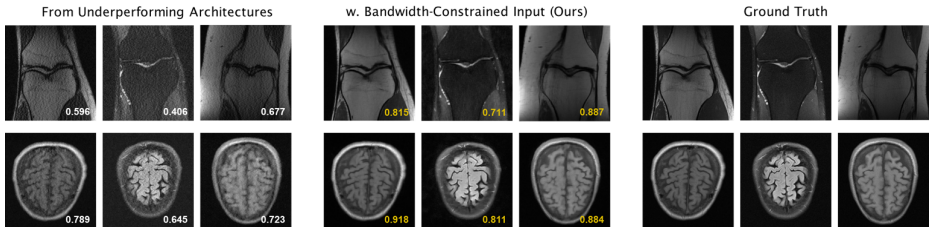


Fig. 1: Example results from underperforming architectures with $4\times$ under-sampling. Turning the left to the right simply by low-pass filtering the white-noise input via a Gaussian blur kernel, which can be implemented as few as *one or two* lines of code. SSIM (\uparrow) values are reported.

are expensive to acquire and could raise issues on robustness and generalization when the acquisition protocol or anatomy changes [23, 24].

Instead of requiring large-scale datasets for capturing prior statistics, the untrained network inspired by deep image prior (DIP) [45] requires only the corrupted or partial measurements and regularizes the reconstruction solely through the inductive biases of its architecture, making it a representative zero-shot self-supervised reconstruction method for a wide range of natural and medical applications [28, 37, 50]. Concretely, DIP parameterizes the unknown desired image via a neural network and optimizes the network parameters such that the output image transformed by the degradation model matches the acquired measurements. Such parameterization is observed to exhibit high resistance to noise and corruption, acting as a form of implicit regularization. Studies have attributed this property to CNN’s inherent spectral bias – the tendency to fit the low-frequency signals before the high-frequency signals (e.g., noise) [5, 41], where the choice of network architecture is often shown to be critically relevant [1, 5, 30].

Despite its great promise, favorable results obtained from the untrained network prior are contingent upon two critical factors: an optimal architecture for a specific task and an early-stopping strategy to prevent overfitting to the noisy, partial measurements. Furthermore, while being agnostic to domain shifts by optimizing on a per-image basis [48], such reconstruction process is inherently slow, hindering its practicality. While these issues are often intertwined — inappropriate and over-parameterized architectures usually exacerbate overfitting and increase runtime, most prior works tackle these challenges separately. For architectural design, existing methods rely on either handcrafting or utilizing neural architecture search techniques [1, 6, 9, 14, 16, 26]. However, the lack of a consensus on the desired architectural prior often leads to a laborious search. Another line of work is dedicated to preventing overfitting through early-stopping [46, 48], subspace optimization [2] or pretraining-then-fine-tuning [3, 35], which also helps shorten the runtime. Similar in spirit to traditional ways of combating overfitting, these methods aim to use fewer trainable parameters with little performance degradation (and may involve costly pretraining) or a held-out subset of measurements for self-validation.

In this work, we explore the possibility of modulating the frequency bias and hence the regularization effects of network priors in an *architecture-agnostic manner*, aiming to enhance a given architecture irrespective of its specific configurations. This is conceivable, in light of the recent body of theoretical and empirical evidence indicating that there are *only a few* key components within the architecture that are driving forces behind the spectral bias in DIP [5, 15, 30, 41]. Inspired by these findings, we develop simple yet effective methods from a frequency perspective to efficiently regularize the network priors, alleviating overfitting by curbing the over-fast convergence of high frequencies, all with minimal architectural modifications and computational costs. Specifically, we propose to (i) constrain the effective bandwidth of the white-noise input via simple spatial blurring or selected Fourier features, (ii) adjust the bandwidths of the interpolation-based upsamplers to control their attenuation (smoothing) extents, and (iii) regularize the Lipschitz constants of the layers to enforce function smoothness. We empirically find that our regularized network priors not only exhibit less vulnerability to overfitting but also tend to achieve better extrapolation and thus higher peak performance in inpainting-like tasks. Demonstrated in the context of MRI reconstruction, our methods significantly improve models across various architectural configurations, largely reducing the need for extensive architectural tuning (Fig. 1). The efficacy of our methods is also showcased in image inpainting and denoising tasks, where the control over frequency is adjusted accordingly. By minimizing architectural influences, our approach additionally offers a unique advantage in efficiency: a **smaller**, previously underperforming network, can now achieve on-par performance or even surpass a **larger**, heavily parameterized high-performing network. Our contributions are three-fold:

- We propose efficient methods that directly modulate the frequency bias in the untrained network priors in an architecture-agnostic manner, effectively addressing challenges related to architecture, overfitting, and runtime in a unified approach.
- The enhanced untrained networks match the performance of leading self-supervised methods and surpass the supervised method especially on out-of-domain data, with up to 86× reduction in runtime (~ 5 mins/slice) for MRI reconstruction, serving as a stronger zero-shot reconstruction baseline than the original DIP scheme.
- Our empirical findings and results on medical and natural image reconstruction tasks shed light on the spectral behaviors of network-based priors—CNNs operating in a single-instance generative setting.

2 Related Work

Function Smoothness and Spectral Bias. Function smoothness, also referred to as function frequency, quantifies how much the output of a function varies with changes in its input [12]. Spectral bias [38, 47] is an implicit bias that favors learning functions changing at a slow rate (low-frequency), e.g., functions with a small Lipschitz constant. In visual domains, this is evident in the network’s output

lacking subtle details. Many regularization techniques shown to aid generalization encourage smoothness implicitly, such as early stopping, ℓ_2 regularizer [39]. Smoothness has been widely used as a model complexity measure in place of model size to account for the well-known "double-descent" phenomenon associated with generalization [34]. To explicitly promote smoothness, it is natural to penalize the norm of the input-output Jacobian [17, 36]. However, due to the high dimensionality of the output such as in accelerated MRI, computation of the Jacobian matrix during training is often intractable. Another efficient and prevalent solution is to constrain the network to be c -Lipschitz with a *pre-defined* Lipschitz constant c [13, 33]. We develop a suitable form of Lipschitz regularization for untrained networks by instead penalizing *learned* Lipschitz constants, with a novel aim of achieving architecture-agnostic untrained image reconstruction.

Input Frequency and Generalization. Input has played an important role in helping neural networks represent signals of various frequencies. As in implicit neural representations (INRs) [42] and neural radiance fields (NeRFs) [32] where coordinates are mapped to RGB values, naively training with raw coordinates as inputs results in over-smoothing; encoding the input coordinates with sinusoidal functions of higher frequencies enables the network to represent higher frequencies [32, 43]. Rahaman et al. [38] also show theoretically and empirically that fitting becomes easier for the network when the input itself contains high-frequency components. However, it has recently been reported that the high-frequency positional input encodings lead to the failure of NeRFs in few-shot settings due to over-fitting [49]. Here, we show that similar issue also applies to untrained network priors and can be efficiently addressed by our methods.

Avoid Overfitting in Untrained Networks. A line of effort has been exclusively devoted to preventing overfitting to noisy images or measurements. Wang et al. [46] propose to track the running variance of the output for an early-stopping criterion, but it is found to be unstable in medical image reconstruction [2]. Yaman et al. [48] propose to split the available measurements into a training and a validation subset and use the latter for self-validation for automated early stopping. Transfer-learning-based untrained networks perform pre-training on synthetic data followed by fine-tuning [3, 35] or subspace optimization [2]. These methods aim to use fewer trainable parameters to avoid overfitting with little performance degradation. In contrast, our methods alleviate overfitting from a frequency perspective and enable significantly better performance while maintaining the same or less model-wise and computation-wise complexity.

3 Method

3.1 Preliminaries

Accelerated MRI The goal of accelerated MRI reconstruction is to recover a desired image $\mathbf{x} \in \mathbb{C}^n$ ($n = n_h \times n_w$) from a set of under-sampled k -space measurements. We focus on a multi-coil scheme in which the forward model is defined as:

$$\mathbf{y}_i = \mathbf{A}_i \mathbf{x} + \epsilon \text{ with } \mathbf{A}_i = \mathbf{MFS}_i, \quad i = 1, \dots, c, \quad (1)$$

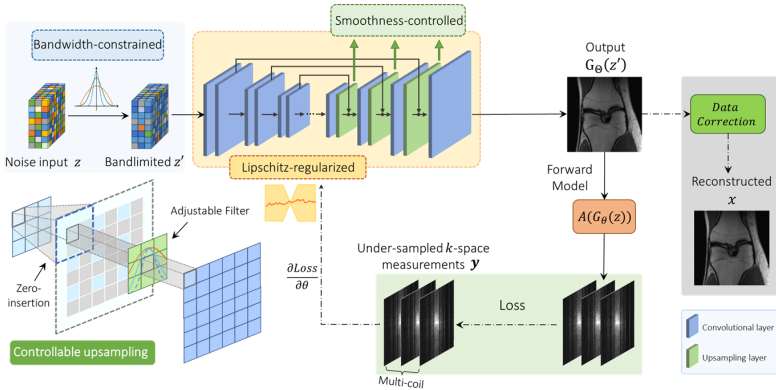


Fig. 2: Overview of the proposed regularized network priors for MRI reconstruction.

where $\mathbf{y}_i \in \mathbb{C}^m$ denotes the k -space measurements from coil i , c denotes the number of coils, $\mathbf{S}_i \in \mathbb{C}^n$ denotes the coil sensitivity map (CSM) that is applied to the image \mathbf{x} through element-wise multiplications, $\mathbf{F} \in \mathbb{C}^{n \times n}$ denotes the 2D discrete Fourier transform, $\mathbf{M} \in \mathbb{C}^{m \times n}$ denotes the under-sampling mask, and $\epsilon \in \mathbb{C}^m$ denotes the measurement noise.

Untrained MRI Reconstruction is often framed as an inpainting problem where the network recovers the unacquired k -space measurements (masked) based on the acquired k -space data (observed). The image \mathbf{x} is parameterized via a neural network $\mathbf{G}_\theta(\mathbf{z})$ with a fixed noise input vector \mathbf{z} drawn from a uniform distribution $z \sim \mathcal{U}(0,1)$. With the aforementioned MRI forward model, the untrained network solves the following optimization problem:

$$\theta^* = \arg \min_{\theta} \mathcal{L}(\mathbf{y}; \mathbf{A}\mathbf{G}_\theta(\mathbf{z})), \quad \mathbf{x}^* = \mathbf{G}_{\theta^*}(\mathbf{z}). \quad (2)$$

Such parameterization allows novel image priors to be designed dependent on the network architecture and the associated parameters. Nevertheless, many studies augment the untrained networks with traditional image regularizers [29], e.g., Total variation (TV), though it can only partially alleviate over-fitting [2, 35]. In our experimental sections, we show that TV is not as effective as ours in improving under-performing architectures.

3.2 Architecture-agnostic Frequency Regularization

To modulate the regularization effects of the network prior, we identify three sources of spectral bias within the network and introduce corresponding regulation methods, as depicted in Fig. 2. Each method requires only minimal hyperparameters to achieve architecture-agnostic control over the network priors.

Bandwidth-constrained Input. An important aspect of untrained networks that can be easily overlooked is their inputs. Conventionally, the inputs are randomly sampled from either a uniform or Gaussian distribution and are then

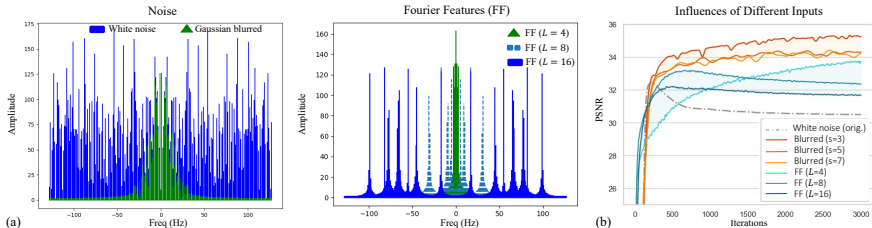


Fig. 3: (a) Visualization of the 1D white noise, the low-passed noise via Gaussian blur, and Fourier features of various frequencies in the frequency domain. (b) Gaussian blurred noise input and Fourier features with lower f_c ($L = 4$ or 8) are both effective in alleviating overfitting and enhancing the peak performance.

mapped to an image. From a frequency perspective, such white-noise input comprises all frequencies with uniform intensities [11]. With this view in mind, we draw an analogy between untrained networks and INRs that map Fourier features to RGB values. Fourier features are sinusoid functions of the input coordinates \mathbf{p} , i.e., $[\sin(2^0\pi\mathbf{p}), \cos(2^0\pi\mathbf{p}), \dots, \sin(2^{L-1}\pi\mathbf{p}), \cos(2^{L-1}\pi\mathbf{p})]$, where a larger L assists the network in representing higher-frequency functions [43]. White noise with variance σ^2 exhibits an autocorrelation that is a scaled Dirac δ -function $\sigma^2\delta(t)$, whose Fourier transform \mathcal{F} has a constant magnitude σ^2 spanning all frequencies μ , i.e., $\mathcal{F}\{\sigma^2\delta(t)\}(\mu) = \sigma^2, \mu \in \mathbb{R}$.

In this sense, an untrained network can be viewed as mapping a broad spectrum of Fourier features to a target image (Fig. 3 (a)). We hypothesize that this enhances the network’s representation ability but likely incurs over-fitting due to the faster convergence of high-frequency components.

To validate this, we applied a Gaussian blur filter $\mathcal{G}_{s,\sigma}$ on the white-noise input z to remove a certain amount of high frequencies before passing it to the network, defined as $z * \mathcal{G}_{s,\sigma}$, where $*$ denotes convolution. The filter size s and sigma value σ that controls the filter’s bandwidth are hyperparameters. As exemplified in Fig. 4, simply adjusting σ already brings significant gains without architectural changes. Similarly, substituting the noise input with Fourier features, with a carefully selected maximum frequency $f_c \propto L$ to limit the input’s effective bandwidth has also proven effective in Fig. 3 (b) and our ablation study (Tab. 2, 3), further validating our hypothesis. Fourier features introduce frequency-diverse input akin to white noise but in a controlled manner, enabling frequency regularization.

Drawing from these empirical findings, we propose to regularize the input’s frequency range, achievable via simple spatial blurring or selected Fourier features,

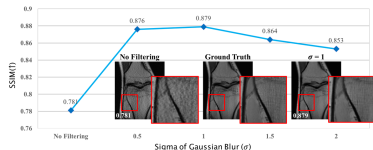


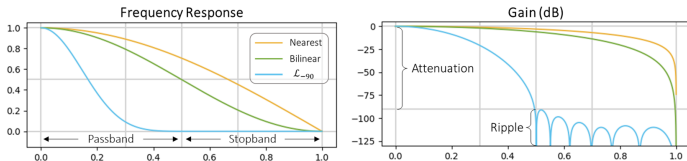
Fig. 4: Narrowing input’s bandwidth enhances performance as a "free lunch". The output becomes smoother as σ increases, up to a certain point.

to efficiently mitigate overfitting and enhance network performance. While Gaussian blur and Fourier Features both offer bandwidth control, they yield different frequency representations (e.g., Fourier features are more *discrete* than Gaussian blurred noise), which may affect performance and susceptibility to parameter tuning differently. We present and compare both results in the experiments.

We note that inputs have been deemed crucial in guiding the generation of the final image not only in INRs but also in generative networks, e.g., transformed Fourier features have been used as an alternative to random input in StyleGAN3 [21], for a different goal of improving the architecture’s equivariance. In contrast, we use a low-passed version of Fourier features or noise input to prevent over-fast convergence on high frequencies and enable better extrapolation. Similar in spirit, recent work by [49] also shows that masking the high-frequency Fourier features helps NeRFs generalize in few-shot settings.

Table 1: Influences of upsamplers on reconstruction. From the left to the right, the attenuation extent of the upsampling method increases. Construction details of the upsampler \mathcal{L}_{-90} follows [30]. Frequency responses of the interpolation filters are shown in the figure below. Evaluated on the $4\times$ fastMRI multi-coil brain datasets.

Methods	w/o. Upsampling.	Nearest	Bilinear	\mathcal{L}_{-90}	# of Params. (Millions)
ConvDecoder [9]	28.69 \pm 1.6	31.78 \pm 1.2	32.31 \pm 1.3	32.48 \pm 1.2	4.1 M
Deep Decoder [14]	24.55 \pm 1.1	27.10 \pm 0.9	31.36 \pm 1.4	32.68 \pm 1.1	0.47 M



Smoothness-controlled Upsampling. We found that constraining the input’s bandwidth significantly enhances shallower architectures, yet the improvement diminishes as the network depth increases. This could partly be attributable to the fact that subsequent layers along with nonlinearity can always generate new arbitrarily high frequencies, as theoretically and empirically proved in [21, 38].

We notice that the interpolation-based upsampling methods within the network, such as nearest neighbor and bilinear, are essentially implicit low-pass filters smoothing out the alias frequencies caused by the increased sampling rate. Prior works [15, 30] on image denoising have shown that these non-trainable upsampling methods are driving forces behind the spectral bias of the network priors, delaying the convergence of higher frequencies. Different upsamplers bias the network towards different spectral properties [30]. We confirm that upsampling also substantially influences image reconstruction and further reveal that an appropriate upsampling method can bridge the performance gap between two distinct architectures (Tab. 1).

Motivated by these results, we introduce a controllable upsampler to modulate the network’s spectral bias, especially the deeper architectures. We achieve this by first interleaving the input feature maps with zeros, and then convolving them with a customized low-pass filter with adjustable bandwidth (Fig. 2). For filter design, we adopt the Kaiser-Bessel window as it offers explicit control over the tradeoffs between passband ripple and stopband attenuation. The Kaiser window is defined as

$$w(n) = I_0(\beta\sqrt{1 - (2n/M)^2})/I_0(\beta), -M/2 \leq n \leq M/2, \quad (3)$$

where M is the desired spatial extent of the window, $\beta \geq 0$ is the shape parameter—the higher it is, the greater the stopband attenuation is (and generally the smoother the image is), and I_0 is the zeroth-order modified Bessel function of the first kind [20]. This plug-and-play upsampler can be inserted in different layers with different M and β hyperparameters, offering flexible and precise control.

Lipschitz-regularized Layers. Spectral bias towards low frequencies favors functions that do not change at a high rate, i.e., functions with small Lipschitz constants. A function $f : \mathcal{X} \rightarrow \mathcal{Y}$ is said to be Lipschitz continuous if there is a constant $k > 0$ such that

$$\|f(x_1) - f(x_2)\|_p \leq k\|x_1 - x_2\|_p \quad \forall x_1, x_2 \in \mathcal{X}, \quad (4)$$

where k is the Lipschitz constant that bounds how fast f can change globally w.r.t. input perturbations.

Instead of upper bounding the Lipschitz constants of the network layers to pre-defined and manually chosen values as in [41], we make the per-layer Lipschitz bounds learnable and regularize their magnitudes during optimization.

The Lipschitz constant of a convolutional layer is bounded by the operator norm of its weight matrix [13]. To bound a convolutional layer to a specific Lipschitz constant k , the layer with m input channels, c output channels and kernels of size $w \times h$ is first reshaped to a 2-D matrix $W^\ell \in \mathbb{R}^{n \times cwh}$, and then normalized as:

$$\tilde{W}_\ell = \frac{W_\ell}{\max(1, \frac{\|W_\ell\|_p}{\text{SoftPlus}(k_\ell)})}, \quad (5)$$

where k_ℓ is a learnable Lipschitz constant for each layer, $\|\cdot\|_p$ is chosen as the ℓ_∞ norm and $\text{SoftPlus}(k_\ell) = \ln(1 + \exp(k_\ell))$ ensures the learned Lipschitz bounds are non-negative. Such formulation *only* normalizes W_ℓ if its matrix norm is larger than the learned Lipschitz constraint during training. Integrating the ultimate Lipschitz regularization with *learned* Lipschitz constants into Eq. (2), our regularized training objective is:

$$\min_{\Theta, \mathbf{K}} \mathcal{L}(\mathbf{y}; \mathbf{A}\mathbf{G}_\Theta(\mathbf{z})) + \lambda \sum_{l=1}^L \text{SoftPlus}(\mathbf{k}_l)^2 \quad (6)$$

where \mathbf{K} is a collection of per-layer learnable Lipschitz constant k_ℓ jointly optimized with the network parameters, and λ controls the granularity of smoothness.

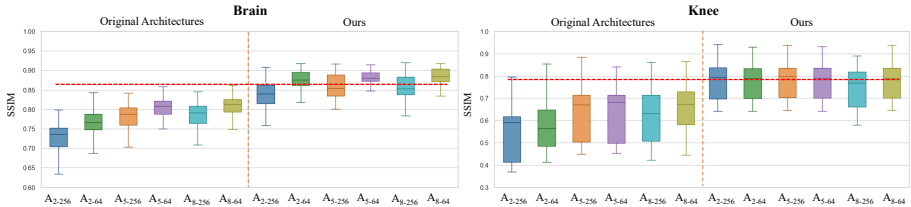


Fig. 5: Our approach significantly minimizes the performance gaps among architectures with various depths $\{2, 5, 8\}$ and widths $\{64, 256\}$.

4 Experiments

4.1 Setup and datasets

We first (1) validate the proposed methods’ effectiveness in enhancing the performance of untrained networks across various architectural configurations, especially those originally underperforming. We then (2) benchmark the enhanced versions of those *compact* architectures against established supervised and self-supervised methods on both in-domain and out-of-domain datasets in terms of accuracy and efficiency. We also (3) compare our methods with self-validation-based early stopping [48] on overcoming overfitting, and show that it is complementary to our approach by further shortening the reconstruction time. Finally, we demonstrate the utility of our methods in (4) general image inpainting and denoising tasks and perform spectral bias analysis on all evaluated tasks.

The MRI experiments were performed on two publicly available datasets including the multi-coil knee and brain MRI images from fastMRI database [25], and multi-coil knee MRI images from Stanford 3D FSE knee dataset [19]. The fully-sampled k -space data was retrospectively masked by selecting 25 central k -space lines along with a uniform undersampling at outer k -space, achieving the standard $4\times$ acceleration. For training the supervised baseline, the knee training set consists of 367 PD and PDFS slices and the brain training set consists of 651 slices with a mixture of T1, T2 weighted images. 50 knee slices and 50 brain slices were sampled from the respective multi-coil validation datasets for evaluation.

4.2 Implementation Details

Without loss of generality, the base architectures considered in our work are N -level encoder-decoder architectures with full skip connections. The architectures are isotropic with the same width and kernel size throughout the layers. All evaluated architectures are trained for 3k iterations using mean absolute error and Adam optimizer [22] with a learning rate of 0.008. Unless otherwise specified, the results at the last iteration are reported. The input is drawn from a uniform distribution $z \sim \mathcal{U}(0, 1)$. The filter size of the Gaussian blur was set to 5 and the sigma value was randomly sampled from $[0.5, 2.0]$ for every slice. M and β for the Kaiser-based upsamplers are chosen to be $\{15 \times N - 1, 5\}$ and $\{5 \times N\}$ for

Table 2: Effectiveness of the methods in bridging performance gaps among different architectures, evaluated on fastMRI **brain** datasets. Bandlimited inputs achieved by Fourier features ($L = 4$ or 8) or Gaussian blur along with Lipschitz regularization improve all architectures, especially the shallower. The proposed Kaiser-based upsampling dramatically improves the deeper architectures. All architectures end up with similarly high performance. The **best** and the **second-best** are highlighted.

Regularizers	\mathbf{A}_{2-256} \mathbf{A}_{2-64} \mathbf{A}_{5-256} \mathbf{A}_{5-64} \mathbf{A}_{8-256} \mathbf{A}_{8-64}						\mathbf{A}_{2-256} \mathbf{A}_{2-64} \mathbf{A}_{5-256} \mathbf{A}_{5-64} \mathbf{A}_{8-256} \mathbf{A}_{8-64}					
	PSNR \uparrow						SSIM \uparrow					
w/o. Reg. (Plain)	29.08	29.41	31.15	31.42	31.27	31.68	0.729	0.761	0.782	0.801	0.784	0.807
TV	29.22	29.61	31.26	31.37	31.32	31.64	0.735	0.764	0.785	0.802	0.787	0.807
Lipschitz Reg.	30.92	29.73	31.47	32.11	31.50	32.03	0.795	0.766	0.792	0.812	0.800	0.820
Fourier features ($L = 16$)	30.57	30.49	31.57	31.77	31.77	32.09	0.786	0.788	0.794	0.813	0.799	0.819
Fourier features ($L = 8$)	31.42	31.98	31.82	32.42	31.60	32.45	0.804	0.833	0.799	0.831	0.795	0.834
Fourier features ($L = 4$)	31.92	32.59	31.87	32.80	31.71	32.86	0.840	0.863	0.799	0.848	0.793	0.844
Gaussian blurred	33.34	32.67	32.14	32.66	32.03	32.92	0.870	0.866	0.811	0.849	0.825	0.849
Gauss. + Lips.	32.90	33.12	32.08	32.83	31.70	33.14	0.855	0.870	0.815	0.851	0.805	0.849
Gauss. + Lips. + Kaiser Up.	32.50	33.10	33.00	33.21	33.09	33.85	0.836	0.874	0.857	0.876	0.858	0.885

Table 3: Evaluated on fastMRI knee datasets.

Regularizers	\mathbf{A}_{2-256} \mathbf{A}_{2-64} \mathbf{A}_{5-256} \mathbf{A}_{5-64} \mathbf{A}_{8-256} \mathbf{A}_{8-64}						\mathbf{A}_{2-256} \mathbf{A}_{2-64} \mathbf{A}_{5-256} \mathbf{A}_{5-64} \mathbf{A}_{8-256} \mathbf{A}_{8-64}					
	PSNR \uparrow						SSIM \uparrow					
w/o. Reg. (Plain)	27.18	27.62	29.16	29.23	28.98	29.35	0.541	0.575	0.628	0.640	0.625	0.644
TV	28.25	27.85	29.33	29.57	29.54	30.01	0.588	0.592	0.635	0.651	0.645	0.687
Lipschitz Reg.	28.41	29.21	29.17	29.79	29.43	30.14	0.601	0.600	0.629	0.651	0.636	0.666
Fourier features ($L = 16$)	28.42	28.97	29.58	30.26	29.76	30.38	0.587	0.622	0.653	0.671	0.661	0.681
Fourier features ($L = 8$)	28.61	29.98	29.86	30.72	29.66	30.89	0.604	0.670	0.669	0.693	0.662	0.703
Fourier features ($L = 4$)	32.02	32.07	29.40	31.13	29.55	31.17	0.775	0.781	0.665	0.718	0.668	0.717
Gaussian blurred	30.87	30.89	30.02	31.24	29.31	30.89	0.739	0.768	0.694	0.748	0.698	0.727
Gaussian blurred + Lips.	31.61	31.93	29.40	31.67	29.82	31.58	0.750	0.776	0.702	0.727	0.697	0.732
Gauss. + Lips. + Kaiser Up.	31.92	31.61	31.78	31.60	31.09	31.73	0.777	0.776	0.778	0.776	0.750	0.768

knee data (N denotes the n th-level), and $\{5 \times N\}$ and $\{5 \times N\}$ for brain data, respectively. λ is set to 1 for Lipschitz regularizer.

4.3 Effectiveness in reducing architectural sensitivity

Fig. 5 gives a quantitative overview of the substantial improvement using our approach in architectures with diverse configurations on both knee and brain datasets. The different results of the original architectures also confirm the influences of architectural choices on performance. Notably, before applying our methods, the deeper and narrower architectures tend to perform better than their counterparts (more in appendix). This trend aligns with previous works [3, 9, 10, 45] where these architectures tend to be favored in inpainting-like tasks. Here we identify particularly their counterparts (i.e., \mathbf{A}_{x-256}) as "underperforming" architectures. As will be shown in our spectral bias analysis in Sec. 4.5 and appendix, these underperforming architectures learn high frequencies more quickly (though this may be desired for other tasks [30]) and are more susceptible to overfitting, incurring severe artifacts in the output (Figs. 6 and 9). When applied with our methods, as detailed in Tab. 2 and Tab. 3, a large boost in performance is observed in all architectures, especially in \mathbf{A}_{2-256} .

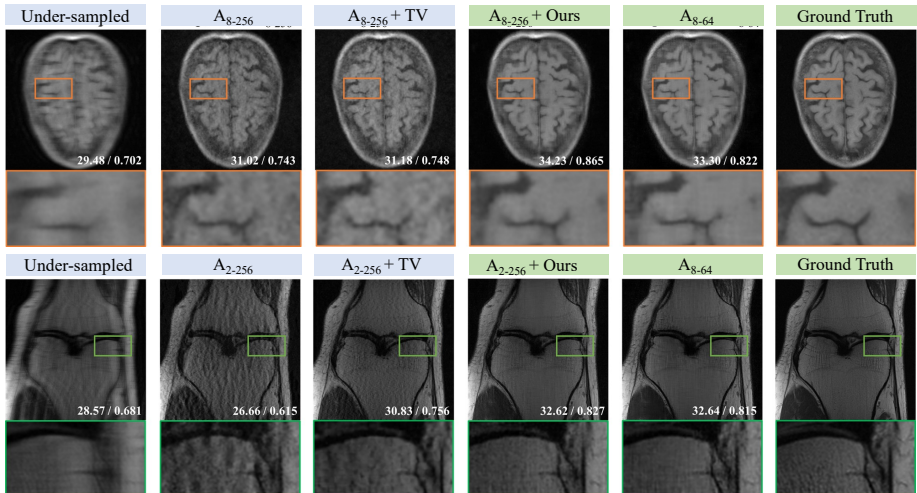


Fig. 6: Our methods enable the underperforming architectures (e.g., \mathbf{A}_{8-256} , \mathbf{A}_{2-256}) to perform similarly to the well-performing architectures (e.g., \mathbf{A}_{8-64}).

We observe that using low-passed inputs via either selected Fourier features or blurring brings the most benefits to the shallower architectures. Better results are achieved when combined with Lipschitz regularization on the layers. On the other hand, deeper architectures benefit more from the Kaiser-based upsampler, which can be seen as performing low-pass filtering on the input feature maps within the network, beyond the initial input layer. We further note that the hyperparameters required for upsampling differ between knee and brain data (Sec. 4.2), with the knee data requiring greater attenuation. This is also consistent with previous findings that they require different numbers of channels for the architecture [9]. Our methods greatly alleviate the need for such architectural tuning by instead allowing for the adjustment of a few key hyperparameters.

4.4 Benchmark results

We then compare our regularized network priors with several established MRI reconstruction methods, including a supervised baseline, a state-of-the-art self-

Table 4: Quantitative results on fastMRI datasets. Runtime: mean (std) per slice.

Datasets	Supervised UNet	CS- ℓ_1 [18]	ZS-SSL [48]	DIP [45]	Deep Decoder [14]	ConvDecoder [9]	\mathbf{A}_{2-64} (vanilla)	\mathbf{A}_{8-64} (vanilla)	\mathbf{A}_{2-64} (Ours)	\mathbf{A}_{8-64} (Ours)	
Brain	PSNR \uparrow	33.35	29.91	34.39	31.15	26.97	31.81	29.42	31.68	33.10	
	SSIM \uparrow	0.889	0.773	0.878	0.782	0.747	0.800	0.761	0.807	0.885	
Knee	PSNR \uparrow	31.15	28.23	32.00	29.16	27.21	29.59	27.62	29.35	32.07	
	SSIM \uparrow	0.776	0.633	0.773	0.628	0.687	0.655	0.575	0.644	0.781	
GFLOPs \downarrow	99.24	-	5461.6	615.72	82.82	699.94	38.42	40.94	62.36	68.38	
Runtime (mins) \downarrow	0.002	-	64.8	14.0	6.6	8.2	5.4	10.5	6.6	12.3	
		(0.00003)	-	(20.18)	(0.61)	(0.63)	(0.35)	(0.47)	(0.62)	(0.58)	(0.65)

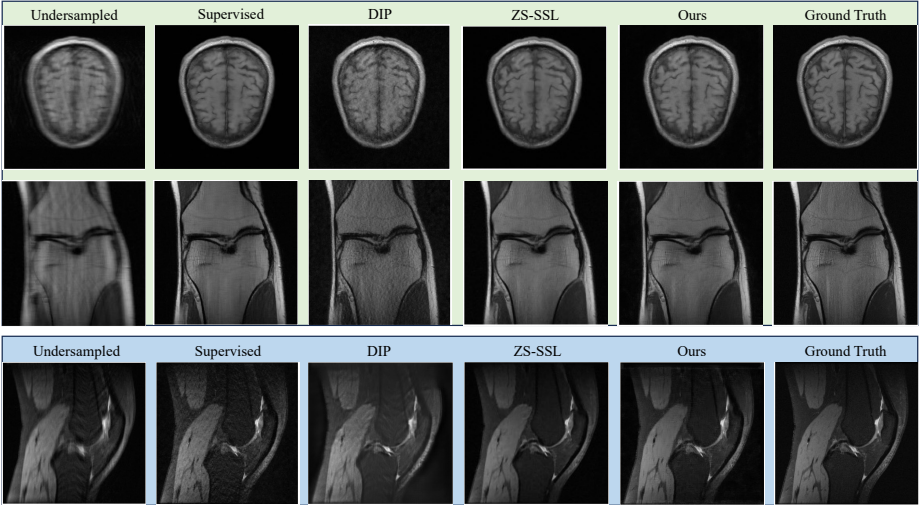


Fig. 7: Qualitative evaluations. **In-domain** : fastMRI. **Out-of-domain** : Stanford FSE.

supervised method (ZS-SSL) [48] and other untrained networks (ConvDecoder [9], Deep Decoder [14]). We adopt two lightweight architectures with distinct configurations as the base model. Visual comparisons are shown in Fig. 7.

Our methods enable the previously underperforming architectures to match the performance of ZS-SSL and the supervised UNet on in-domain fastMRI knee data (Tab. 4) and surpass the trained UNet on out-of-domain Stanford 3D FSE data (Tab. 5) as untrained methods are agnostic to domain shifts. The datasets for training the UNet contain 367 knee slices and 651 brain slices, respectively, covering various kinds of contrast weightings. Our enhanced networks also clearly outperform other untrained networks and the compressed-sensing (CS) based reconstruction. These results demonstrate the benefits of enhancing the untrained methods for generalizable reconstruction. ZS-SSL is an unrolling-based method where the network, i.e., a ResNet [44], is adopted as a denoiser. Comparisons with its UNet-variant, i.e., ZS-SSL-UNet, are included in the appendix. Additionally,

Table 5: Out-of-domain evaluation among supervised and untrained methods and comparisons with self-validation-based early stopping [48].

Method		In-domain		Out-domain		Runtime (mean±std)	
		PSNR	SSIM	PSNR	SSIM	Train	Inference
Trained	U-Net	31.16	0.776	29.16	0.724	~1.5 days	0.1 ± 0.003 sec
Untrained	CS- ℓ_1 [18]	28.23	0.633	22.46	0.407	–	–
	ZS-SSL [48]	32.00	0.773	31.74	0.805	–	26.1 ± 3.5 mins
	DIP [45]	29.16	0.628	28.89	0.664	–	9.2 ± 0.3 mins
	A₂₋₆₄	27.62	0.575	26.03	0.550	–	5.5 ± 0.1 mins
	A₂₋₆₄ w. Self-Val	29.59	0.695	27.59	0.641	–	0.2 ± 0.2 mins
	A₂₋₆₄ (Ours)	32.07	0.781	31.43	0.790	–	6.4 ± 0.4 mins
	A₂₋₆₄ (Ours) w. Self-Val.	31.97	0.776	31.30	0.800	–	0.3 ± 0.1 mins

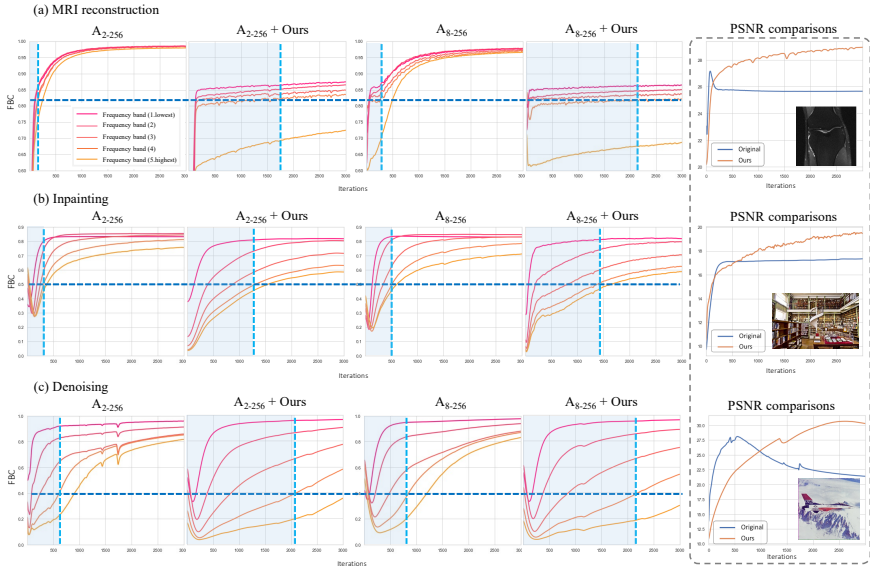


Fig. 8: Measurement of the spectral bias. Our methods allow high frequencies to be fitted at a later iteration, alleviating overfitting and generally beneficial to inpainting-like tasks (i.e., MRI) with higher peak performance. PSNR shown for \mathbf{A}_{2-256} .

ZS-SSL uses a self-validation strategy for early stopping. We further compare it with our methods. Tab. 5 shows that self-validation is not as effective as ours. This is because, while self-validation mitigates overfitting by stopping near the peak PSNR, it does not fundamentally address the issues of underperforming architectures, i.e., the peak PSNR remains subpar. Our methods alleviate overfitting while generally enhancing the peak performance (e.g., Fig. 3), which we further analyze in the next section. Hence, self-validation-based early stopping is complementary to our goal of reducing the architectural sensitivity, and can be integrated into our approach to further shorten the reconstruction time as shown in Tab. 5. Overall, our enhanced network priors achieve comparable performance than ZS-SSL while being orders of magnitude faster.

4.5 Spectral bias analysis

To examine the efficacy of the proposed methods on frequency control over the network, we measure the spectral bias using the metric— frequency-band correspondence (FBC) [41] that calculates the element-wise $|\mathcal{F}(x)|/|\mathcal{F}(y)|$ between the output x and target image y , categorizes it into five frequency bands radially and computes the per-band averages. Higher values indicate higher correspondence. We trace the evolutions of FBC for \mathbf{A}_{8-256} and \mathbf{A}_{2-256} and the corresponding PSNR curves throughout the training iterations in three different tasks.

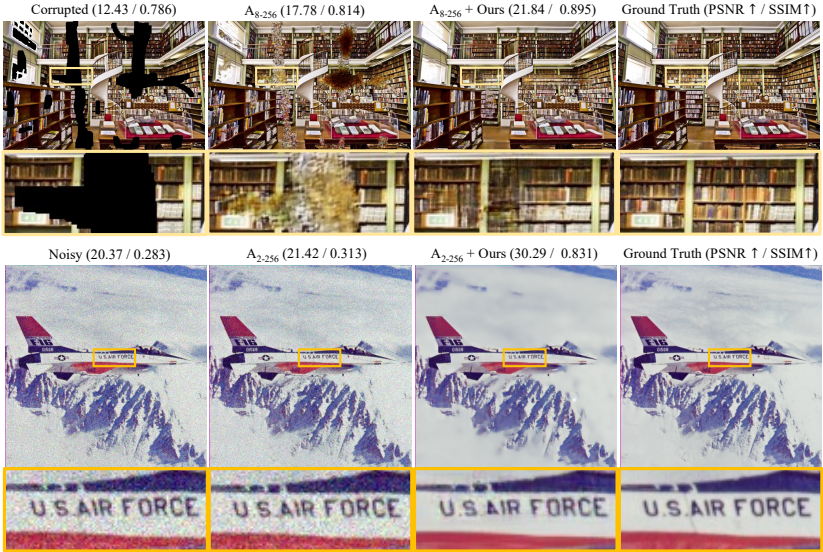


Fig. 9: Inpainting and denoising ($\sigma = 25$) experiments for demonstrating the improvement on underperforming architectures.

As shown in Fig. 8, the original architectures tend to readily fit all frequencies, especially \mathbf{A}_{2-256} , corresponding to its worst performance among all compared architectures. Our methods delay the convergence of higher frequencies in both architectures across all three tasks as designed, which generally leads to higher peak performance for inpainting-like tasks. We hypothesize that a bias towards lower frequencies helps the model leverage spatial information for improved inter/extrapolation capabilities. Qualitative results in Fig. 9 validate our hypothesis. Given that MRI reconstruction resembles an inpainting task for k -space measurements, we expect similar improvement using our regularized network priors, as proved in our experiments. Note that although a stronger spectral bias may not always be optimal, the hyperparameters of our methods enable flexible adaptations for the specific task (more experiments in the appendix).

5 Conclusion

We introduce efficient, architecture-agnostic methods for frequency control over the network priors, offering a novel solution to simultaneously address the key challenges present in untrained image reconstruction. Our approach requires only minimal modifications to the original DIP scheme while achieving significant gains in accuracy and efficiency as evidenced in MRI reconstruction and natural image restoration tasks, making it a stronger zero-shot *baseline* reconstructor with the potential for seamless integration with other advancements in self-supervised reconstruction.

References

1. Arican, M.E., Kara, O., Bredell, G., Konukoglu, E.: Isnas-dip: Image-specific neural architecture search for deep image prior. In: Proceedings of the IEEE/CVF Conference on Computer Vision and Pattern Recognition. pp. 1960–1968 (2022) [2](#)
2. Barbano, R., Antorán, J., Leuschner, J., Hernández-Lobato, J.M., Kereta, Ž., Jin, B.: Fast and painless image reconstruction in deep image prior subspaces. arXiv preprint arXiv:2302.10279 (2023) [2](#), [4](#), [5](#)
3. Barbano, R., Leuschner, J., Schmidt, M., Denker, A., Hauptmann, A., Maass, P., Jin, B.: An educated warm start for deep image prior-based micro ct reconstruction. IEEE Transactions on Computational Imaging (2022) [2](#), [4](#), [10](#)
4. Cao, H., Wang, Y., Chen, J., Jiang, D., Zhang, X., Tian, Q., Wang, M.: Swin-unet: Unet-like pure transformer for medical image segmentation. In: European conference on computer vision. pp. 205–218. Springer (2022) [20](#)
5. Chakrabarty, P., Maji, S.: The spectral bias of the deep image prior. arXiv preprint arXiv:1912.08905 (2019) [2](#), [3](#), [23](#)
6. Chen, Y.C., Gao, C., Robb, E., Huang, J.B.: Nas-dip: Learning deep image prior with neural architecture search. In: European Conference on Computer Vision. pp. 442–459. Springer (2020) [2](#)
7. Cheng, Z., Gadelha, M., Maji, S., Sheldon, D.: A bayesian perspective on the deep image prior. In: Proceedings of the IEEE/CVF Conference on Computer Vision and Pattern Recognition. pp. 5443–5451 (2019) [18](#), [19](#)
8. Dabov, K., Foi, A., Egiazarian, K.: Video denoising by sparse 3d transform-domain collaborative filtering [c]. In: Proc. 15th European Signal Processing Conference. vol. 1, p. 7 (2007) [25](#)
9. Darestani, M.Z., Heckel, R.: Accelerated mri with un-trained neural networks. IEEE Transactions on Computational Imaging **7**, 724–733 (2021) [2](#), [7](#), [10](#), [11](#), [12](#), [22](#)
10. Darestani, M.Z., Liu, J., Heckel, R.: Test-time training can close the natural distribution shift performance gap in deep learning based compressed sensing. In: International Conference on Machine Learning. pp. 4754–4776. PMLR (2022) [10](#)
11. E Woods, R., C Gonzalez, R.: Digital image processing (2008) [6](#)
12. Fridovich-Keil, S., Gontijo Lopes, R., Roelofs, R.: Spectral bias in practice: The role of function frequency in generalization. Advances in Neural Information Processing Systems **35**, 7368–7382 (2022) [3](#)
13. Gouk, H., Frank, E., Pfahringer, B., Cree, M.J.: Regularisation of neural networks by enforcing lipschitz continuity. Machine Learning **110**, 393–416 (2021) [4](#), [8](#)
14. Heckel, R., Hand, P.: Deep decoder: Concise image representations from untrained non-convolutional networks. arXiv preprint arXiv:1810.03982 (2018) [2](#), [7](#), [11](#), [12](#), [22](#)
15. Heckel, R., Soltanolkotabi, M.: Denoising and regularization via exploiting the structural bias of convolutional generators. International Conference on Representation Learning (2020) [3](#), [7](#), [19](#)
16. Ho, K., Gilbert, A., Jin, H., Collomosse, J.: Neural architecture search for deep image prior. Computers & Graphics **98**, 188–196 (2021) [2](#)
17. Hoffman, J., Roberts, D.A., Yaida, S.: Robust learning with jacobian regularization. arXiv preprint arXiv:1908.02729 (2019) [4](#)
18. Jaspán, O.N., Fleysher, R., Lipton, M.L.: Compressed sensing mri: a review of the clinical literature. The British journal of radiology **88**(1056), 20150487 (2015) [11](#), [12](#)
19. K, E., Am, S., M, L., M, A., M., U.: Creation of fully sampled mr data repository for compressed sensing of the knee [9](#)

20. Kaiser, J.: Nonrecursive digital filter design using the $i0$ -sinh window function, paper presented at symposium on circuits and systems, inst. of electr. and electron. In Proc. 1974 IEEE International Symposium on Circuits & Systems, pages 20-23, 1974 (1974) [8](#)
21. Karras, T., Aittala, M., Laine, S., Härkönen, E., Hellsten, J., Lehtinen, J., Aila, T.: Alias-free generative adversarial networks. *Advances in Neural Information Processing Systems* **34**, 852–863 (2021) [7](#)
22. Kingma, D.P., Ba, J.: Adam: A method for stochastic optimization. arXiv preprint arXiv:1412.6980 (2014) [9](#)
23. Knoll, F., Hammernik, K., Kobler, E., Pock, T., Recht, M.P., Sodickson, D.K.: Assessment of the generalization of learned image reconstruction and the potential for transfer learning. *Magnetic resonance in medicine* **81**(1), 116–128 (2019) [2](#)
24. Knoll, F., Murrell, T., Sriram, A., Yakubova, N., Zbontar, J., Rabbat, M., Defazio, A., Muckley, M.J., Sodickson, D.K., Zitnick, C.L., et al.: Advancing machine learning for mr image reconstruction with an open competition: Overview of the 2019 fastmri challenge. *Magnetic resonance in medicine* **84**(6), 3054–3070 (2020) [2](#), [23](#)
25. Knoll, F., Zbontar, J., Sriram, A., Muckley, M.J., Bruno, M., Defazio, A., Parente, M., Geras, K.J., Katsnelson, J., Chandarana, H., et al.: fastmri: A publicly available raw k-space and dicom dataset of knee images for accelerated mr image reconstruction using machine learning. *Radiology: Artificial Intelligence* **2**(1), e190007 (2020) [9](#), [22](#)
26. Korkmaz, Y., Dar, S.U., Yurt, M., Özbey, M., Cukur, T.: Unsupervised mri reconstruction via zero-shot learned adversarial transformers. *IEEE Transactions on Medical Imaging* (2022) [2](#)
27. Lingala, S.G., Hu, Y., DiBella, E., Jacob, M.: Accelerated dynamic mri exploiting sparsity and low-rank structure: kt slr. *IEEE transactions on medical imaging* **30**(5), 1042–1054 (2011) [1](#)
28. Liu, D., Wang, J., Shan, Q., Smyl, D., Deng, J., Du, J.: Deepeit: deep image prior enabled electrical impedance tomography. *IEEE Transactions on Pattern Analysis and Machine Intelligence* (2023) [2](#)
29. Liu, J., Sun, Y., Xu, X., Kamilov, U.S.: Image restoration using total variation regularized deep image prior. In: ICASSP 2019-2019 IEEE International Conference on Acoustics, Speech and Signal Processing (ICASSP). pp. 7715–7719. IEEE (2019) [5](#)
30. Liu, Y., Li, J., Pang, Y., Nie, D., Yap, P.T.: The devil is in the upsampling: Architectural decisions made simpler for denoising with deep image prior. In: Proceedings of the IEEE/CVF International Conference on Computer Vision. pp. 12408–12417 (2023) [2](#), [3](#), [7](#), [10](#), [19](#), [20](#), [23](#)
31. Lustig, M., Donoho, D., Pauly, J.M.: Sparse mri: The application of compressed sensing for rapid mr imaging. *Magnetic Resonance in Medicine: An Official Journal of the International Society for Magnetic Resonance in Medicine* **58**(6), 1182–1195 (2007) [1](#)
32. Mildenhall, B., Srinivasan, P.P., Tancik, M., Barron, J.T., Ramamoorthi, R., Ng, R.: Nerf: Representing scenes as neural radiance fields for view synthesis. *Communications of the ACM* **65**(1), 99–106 (2021) [4](#)
33. Miyato, T., Kataoka, T., Koyama, M., Yoshida, Y.: Spectral normalization for generative adversarial networks. arXiv preprint arXiv:1802.05957 (2018) [4](#)
34. Nakkiran, P., Kaplun, G., Bansal, Y., Yang, T., Barak, B., Sutskever, I.: Deep double descent: Where bigger models and more data hurt. *Journal of Statistical Mechanics: Theory and Experiment* **2021**(12), 124003 (2021) [4](#)

35. Nittscher, M., Lameter, M., Barbano, R., Leuschner, J., Jin, B., Maass, P.: Svd-dip: Overcoming the overfitting problem in dip-based ct reconstruction. arXiv preprint arXiv:2303.15748 (2023) [2](#), [4](#), [5](#)
36. Novak, R., Bahri, Y., Abolafia, D.A., Pennington, J., Sohl-Dickstein, J.: Sensitivity and generalization in neural networks: an empirical study. arXiv preprint arXiv:1802.08760 (2018) [4](#)
37. Qayyum, A., Ilahi, I., Shamshad, F., Boussaid, F., Bennamoun, M., Qadir, J.: Untrained neural network priors for inverse imaging problems: A survey. IEEE Transactions on Pattern Analysis and Machine Intelligence (2022) [2](#)
38. Rahaman, N., Baratin, A., Arpit, D., Draxler, F., Lin, M., Hamprecht, F., Bengio, Y., Courville, A.: On the spectral bias of neural networks. In: International Conference on Machine Learning. pp. 5301–5310. PMLR (2019) [3](#), [4](#), [7](#), [24](#)
39. Rosca, M., Weber, T., Gretton, A., Mohamed, S.: A case for new neural network smoothness constraints. In: Zosa Forde, J., Ruiz, F., Pradier, M.F., Schein, A. (eds.) Proceedings on "I Can't Believe It's Not Better!" at NeurIPS Workshops. Proceedings of Machine Learning Research, vol. 137, pp. 21–32. PMLR (12 Dec 2020), <https://proceedings.mlr.press/v137/rosca20a.html> [4](#)
40. Schwarz, K., Liao, Y., Geiger, A.: On the frequency bias of generative models. Advances in Neural Information Processing Systems **34**, 18126–18136 (2021) [22](#)
41. Shi, Z., Mettes, P., Maji, S., Snoek, C.G.: On measuring and controlling the spectral bias of the deep image prior. International Journal of Computer Vision **130**(4), 885–908 (2022) [2](#), [3](#), [8](#), [13](#), [18](#)
42. Sitzmann, V., Martel, J., Bergman, A., Lindell, D., Wetzstein, G.: Implicit neural representations with periodic activation functions. Advances in neural information processing systems **33**, 7462–7473 (2020) [4](#)
43. Tancik, M., Srinivasan, P., Mildenhall, B., Fridovich-Keil, S., Raghavan, N., Singhal, U., Ramamoorthi, R., Barron, J., Ng, R.: Fourier features let networks learn high frequency functions in low dimensional domains. Advances in Neural Information Processing Systems **33**, 7537–7547 (2020) [4](#), [6](#)
44. Timofte, R., Agustsson, E., Van Gool, L., Yang, M.H., Zhang, L.: Ntire 2017 challenge on single image super-resolution: Methods and results. In: Proceedings of the IEEE conference on computer vision and pattern recognition workshops. pp. 114–125 (2017) [12](#)
45. Ulyanov, D., Vedaldi, A., Lempitsky, V.: Deep image prior. In: Proceedings of the IEEE conference on computer vision and pattern recognition. pp. 9446–9454 (2018) [2](#), [10](#), [11](#), [12](#)
46. Wang, H., Li, T., Zhuang, Z., Chen, T., Liang, H., Sun, J.: Early stopping for deep image prior. arXiv preprint arXiv:2112.06074 (2021) [2](#), [4](#)
47. Xu, Z.Q.J., Zhang, Y., Xiao, Y.: Training behavior of deep neural network in frequency domain. In: Neural Information Processing: 26th International Conference, ICONIP 2019, Sydney, NSW, Australia, December 12–15, 2019, Proceedings, Part I 26. pp. 264–274. Springer (2019) [3](#)
48. Yaman, B., Hosseini, S.A.H., Akçakaya, M.: Zero-shot self-supervised learning for mri reconstruction. International Conference on Learning Representations (2022) [2](#), [4](#), [9](#), [11](#), [12](#), [25](#), [26](#)
49. Yang, J., Pavone, M., Wang, Y.: Freenerf: Improving few-shot neural rendering with free frequency regularization. In: Proceedings of the IEEE/CVF Conference on Computer Vision and Pattern Recognition. pp. 8254–8263 (2023) [4](#), [7](#)
50. Yu, T., Hilbert, T., Piredda, G.F., Joseph, A., Bonanno, G., Zenkhri, S., Omoumi, P., Cuadra, M.B., Canales-Rodríguez, E.J., Kober, T., et al.: Validation and gener-

alizability of self-supervised image reconstruction methods for undersampled mri. arXiv preprint arXiv:2201.12535 (2022) 2

Appendix

A Natural image experiments

A.1 Inpainting

To the best of our knowledge, our method is the first attempt that addresses challenges related to architecture, overfitting and runtime simultaneously.

To compare with prior DIP methods, we 1) first employ the network configurations that work best in their respective settings [7, 41], i.e., the architectures used are different in different methods, as shown in Fig. 10 and Fig. 11, we then 2) use an underperforming architecture for all competing methods, as shown in Fig. 12.

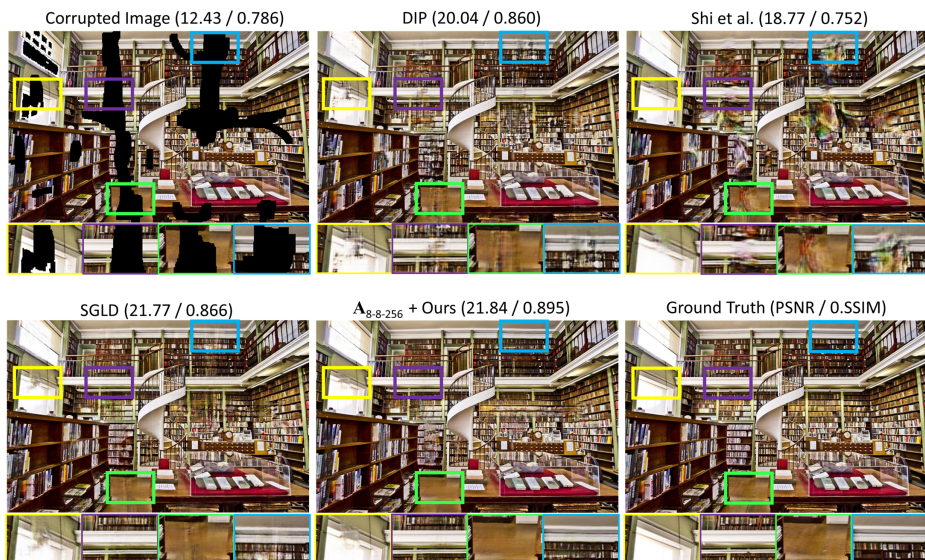


Fig. 10: Qualitative comparisons with previous DIP methods on inpainting.

A.2 Denoising

We first show the results when each method operates in its original setting (Fig. 13), and then evaluate them when an unsuitable architecture is used (Fig. 14).

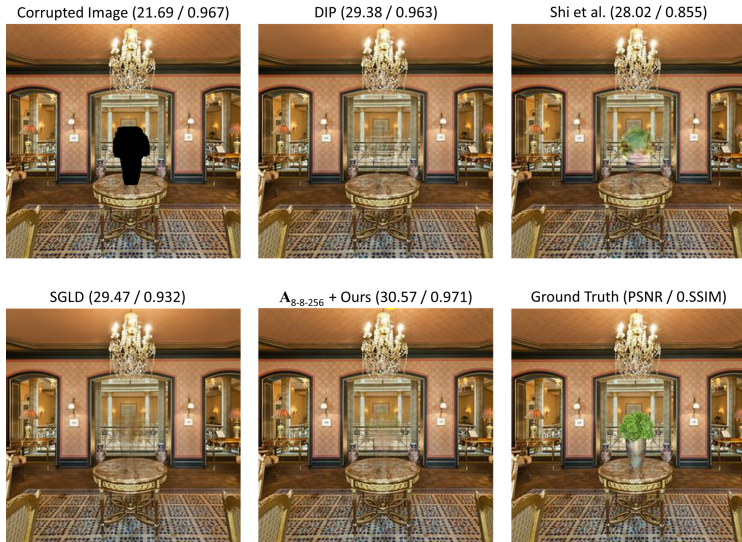


Fig. 11: Qualitative comparisons with previous DIP methods.



Fig. 12: When unsuitable architectures are used, e.g., UNet w. deconvolutions, ResNet w/o. upsampling, SGLD [7] fails to perform restoration. This confirms the importance of architectural decisions in DIP, and that previous methods do not address the architecture-related challenges. Note that deconvolutions have been reported to be not suitable for DIPs [15, 30]. Similarly for ResNet, which does not have any upsampling layers [30].



Fig. 13: Qualitative comparisons with previous DIP methods on denoising. Ours trades off the metrics for sharpness.

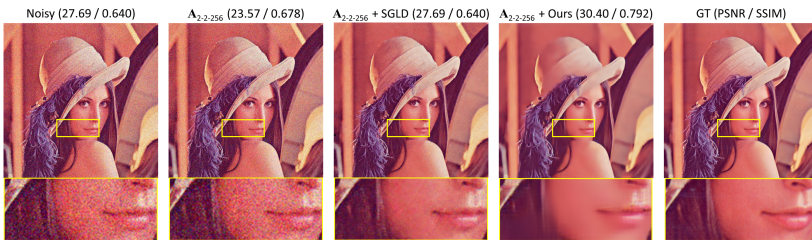


Fig. 14: Denoising results. The base network used in each competing method is replaced by an underperforming architecture, i.e., A_{2-256} .

Transformer. Besides CNN, we show here the result on Swin U-Net [4], which consists of only Swin Transformer blocks and skip connections, i.e., no upsampling is involved. As noted in a recent study [30], the unlearnt upsampling is the driving force behind the spectral bias of DIP, and such transformers are more difficult to perform denoising. This finding assumes the white noise as the input. Here, we show that constraining the bandwidth of the noise input enables long-lasting denoising even in such models.

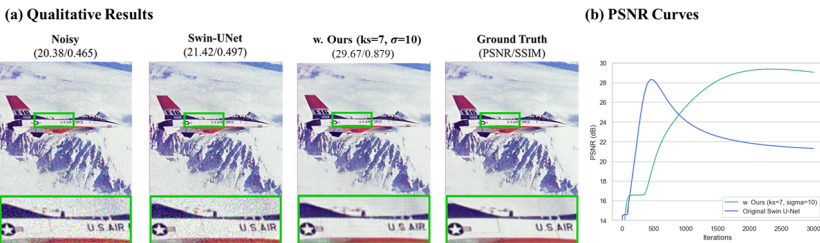


Fig. 15: Qualitative denoising results of a transformer [4]. Our method substantially alleviates the overfitting and enhances the peak PSNR.

B Influences of hyperparameters

As our methods contain several hyperparameters, we visualize their influences on the frequency control and hence the regularization effects over the output image in Fig. 16.

s and σ are associated with the Gaussian blur kernel applied on the noise input. The larger the s and/or σ is, the more high frequencies are removed from the noise input (i.e., the smoother the output is). M and β are for adjusting the attenuation extents of the Kaiser-based upsamplers. The higher the M and/or β is, the larger the attenuation of the high-frequency replica (i.e., the smoother the output is).

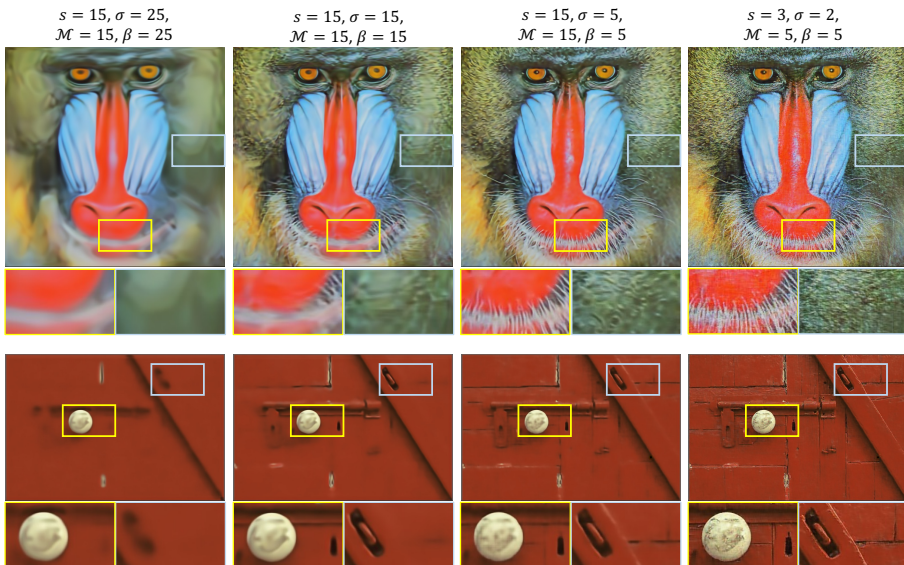


Fig. 16: Visualizations of the frequency control with our methods in denoising experiments.

C Comparisons with early-stopping

To complement Table 5 in the main text, here we visualize in Fig. 17 that early stopping, even though prevents further performance decay, cannot fundamentally improve the underperforming architectures. In other words, **early stopping could not cope with ill-designed architectures**.

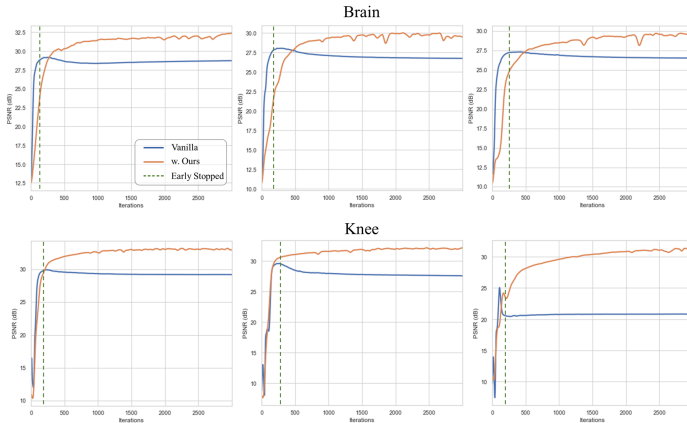


Fig. 17: Comparisons with self-validation-based early stopping. Although early stopping alleviates overfitting, it cannot fundamentally improve the underperforming architectures. Our methods can improve their peak performance while also mitigating overfitting.

D Architectural influences

To better inform our method design, we 1) investigate the architectural influences in the context of MRI reconstruction, and also 2) validate our findings on image inpainting and denoising. **Our results confirm that the reconstruction outcome is sensitive to basic architectural properties.**

D.1 Crucial Architectural Elements

We first pinpointed the *core* architecture elements that have a critical impact on the performance.

Experimental setup i. Since a decoder is the minimum requirement for reconstruction, we experimented with two types of 7-layered decoder-only architectures, i.e., ConvDecoder [9] and Deep Decoder [14]. Experiments were performed on the $4\times$ under-sampled multi-coil knee MRI from fastMRI database [25].

Upsampling (interpolation filter). Fig. 18(a) suggests an interesting result: removing the *unlearned* upsampling, e.g., bilinear, leads to either failure or unstable results (see gray curves). Unlike transposed convolution, the unlearned upsampler is essentially a *fixed* low-pass interpolation filter that attenuates the introduced high-frequency replica and also the signal. Frequency response of bilinear interpolation filter decays more rapidly than that of nearest neighbor as the frequency increases (Fig. 18 (b)), suggesting stronger attenuation and smoothing effects. Hence, bilinear upsampling typically biases the network towards generating smoother outputs, as prevalent in generative models [40]. Transposed convolutions, however, are not guaranteed to be low-passed as they are *learnable*. Due to the spectral bias of network layers, they may be low-passed during early

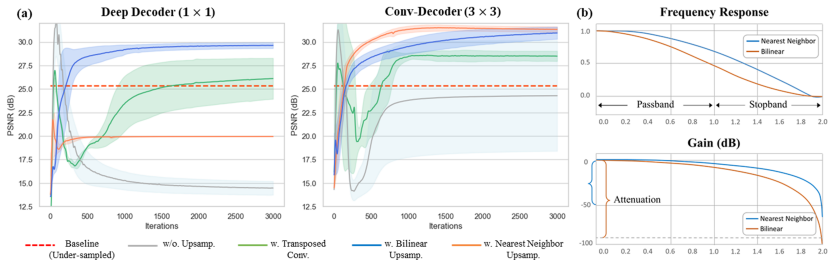


Fig. 18: Influences of architectural elements. Results averaged across three different widths.

training to still enable reconstruction, but the results could be unstable (green curves).

Convolutional layers. When the unlearned upsampling operations are absent, ConvDecoder (3×3) still enables reconstruction while Deep Decoder (1×1) fails completely (Fig. 18(a)). A similar phenomenon is also reported in image denoising [5, 30]. This again can be attributed to CNN’s inherent spectral bias and suggests that the size of the kernel also matters, further corroborated in Tab. 7.

Discussion. Results of this pilot experiment suggest that the spatial kernels with low-pass characteristics, either learnable or unlearned, are *crucial* to the success of untrained network priors. In particular, bilinear upsampling with a fixed low-pass filter produces more stable and better results (blue curves).

D.2 Depth, Width and Skip Connections

Here, we demonstrate that insights gained about the unlearned upsampling can aid in understanding the connection between architectural characteristics and the reconstruction task.

Experimental setup ii. For this large-scale validation, we experimented with an isotropic encoder-decoder architecture used in the original DIP, i.e., equal width and kernel size for all layers throughout the network. Design choices are detailed in Tab. 6. Experiments were performed on the publicly available $4 \times$ under-sampled multi-coil knee MRI from fastMRI database [24].

Table 6: Test bed for studying the architectural influences of an encoder-decoder untrained networks.

Archi. Type	Depth (d)	# of Skips (s)	Width (w)	Kernel Size (k)
$\mathbf{A}_{d-s-w-k}$	{2-L, 3-L, 4-L, 5-L, 8-L}	{zero, half, full}	{32, 64, 128, 256}	{ $3 \times 3, 5 \times 5$ }

What do deeper and narrower architectures produce? (Tab. 7). Theoretically, as the number of layers (depth) or channels (width) increases, the ability of the network to learn arbitrarily high frequencies (details, noise) is typically

Table 7: Influences of typical architectural design choices in knee reconstruction. *Deeper* and/or *Narrower* architectures tend to perform better; skip connections influence the deep architectures more; larger kernels perform slightly better. $\mathbf{A}_{8\text{-full-}32\text{-}3}$ performs the best (in **lime**); $\mathbf{A}_{2\text{-full-}256\text{-}3}$ performs the worst (in **red**).

		Width (↓)															
		Archi.		PSNR SSIM		Archi.		PSNR SSIM		Archi.		PSNR SSIM					
Depth (↑)		$\mathbf{A}_{2\text{-full-}256\text{-}3}$		26.67	0.530	$\mathbf{A}_{2\text{-full-}128\text{-}3}$		27.12	0.543	$\mathbf{A}_{2\text{-full-}64\text{-}3}$		27.70	0.583	$\mathbf{A}_{2\text{-full-}32\text{-}3}$		28.47	0.641
		$\mathbf{A}_{3\text{-full-}256\text{-}3}$		28.22	0.590	$\mathbf{A}_{3\text{-full-}128\text{-}3}$		28.59	0.605	$\mathbf{A}_{3\text{-full-}64\text{-}3}$		28.55	0.616	$\mathbf{A}_{3\text{-full-}32\text{-}3}$		29.25	0.660
		$\mathbf{A}_{4\text{-full-}256\text{-}3}$		28.68	0.617	$\mathbf{A}_{4\text{-full-}128\text{-}3}$		28.95	0.622	$\mathbf{A}_{4\text{-full-}64\text{-}3}$		28.87	0.624	$\mathbf{A}_{4\text{-full-}32\text{-}3}$		29.70	0.671
		$\mathbf{A}_{5\text{-full-}256\text{-}3}$		28.61	0.613	$\mathbf{A}_{5\text{-full-}128\text{-}3}$		28.87	0.615	$\mathbf{A}_{5\text{-full-}64\text{-}3}$		29.33	0.648	$\mathbf{A}_{5\text{-full-}32\text{-}3}$		29.81	0.680
		$\mathbf{A}_{8\text{-full-}256\text{-}3}$		28.98	0.625	$\mathbf{A}_{8\text{-full-}128\text{-}3}$		29.33	0.637	$\mathbf{A}_{8\text{-full-}64\text{-}3}$		29.45	0.651	$\mathbf{A}_{8\text{-full-}32\text{-}3}$		30.04	0.695
		Skip Connections (–)				Kernel Size (↑)											
		$\mathbf{A}_{2\text{-half-}256\text{-}3}$		26.91	0.535	$\mathbf{A}_{2\text{-zero-}256\text{-}3}$		26.83	0.535	$\mathbf{A}_{2\text{-full-}256\text{-}3}$		26.67	0.530	$\mathbf{A}_{2\text{-full-}256\text{-}5}$		26.98	0.550
		$\mathbf{A}_{4\text{-half-}256\text{-}3}$		28.55	0.621	$\mathbf{A}_{4\text{-zero-}256\text{-}3}$		27.54	0.697	$\mathbf{A}_{5\text{-full-}256\text{-}3}$		28.61	0.613	$\mathbf{A}_{5\text{-full-}256\text{-}5}$		28.82	0.624
		$\mathbf{A}_{8\text{-half-}256\text{-}3}$		29.12	0.669	$\mathbf{A}_{8\text{-zero-}256\text{-}3}$		28.51	0.609	$\mathbf{A}_{8\text{-full-}256\text{-}3}$		28.98	0.625	$\mathbf{A}_{8\text{-full-}256\text{-}5}$		29.12	0.634

increased [38]. While this is true for width, we have found that the effect on depth turns out to be attenuated by unlearned upsampling. As evidenced in Fig. 19, deeper architectures typically generate smoother images, exhibiting a stronger preference for low-frequency information, whereas shallower counterparts, *even though they have fewer parameters*, are more susceptible to noise and overfitting (**red arrows**). This is more evident when comparing the *same* architectures with just different upsamplers, where the architectures with bilinear upsampling (stronger attenuation) are less prone to overfitting than the ones using nearest neighbor (NN) upsampling (**cyan** vs. **blue**). Hence, it is not merely the number of parameters but the architectural characteristics promoting low frequencies that seem to be the primary reason for the high performance. Note that all these results are only achievable when *unlearned* upsampling is involved (gray dashed curves).

Skip connections. Deep architectures with zero skip connection converge more slowly and may lead to over-smoothing as shown in Fig. 19 (**red curves**). Skip connections greatly alleviate this issue and introduce more details (**cyan curves**), which we speculate could be due to the "reduced effective up-sampling rate". Yet, excessive skip connections make a deep architecture behave similarly as a shallower one, generating more noise (Fig. 19 right). Overall, they exert a greater influence on deeper architectures ($\mathbf{A}_{8\text{-zero}} < \mathbf{A}_{8\text{-full}} < \mathbf{A}_{8\text{-half}}$) compared to shallower ones ($\mathbf{A}_{2\text{-full}} \approx \mathbf{A}_{2\text{-zero}}$).

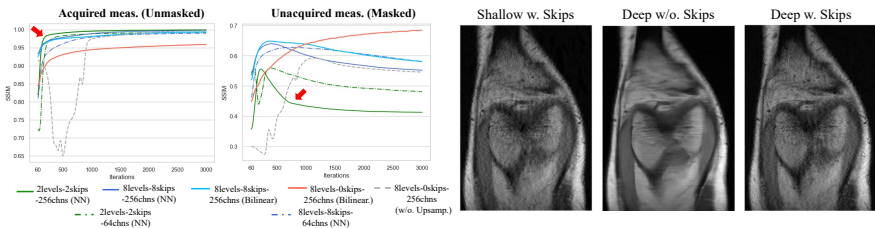


Fig. 19: Generalizability of different architectures on the masked regions.

D.3 Validations on image denoising and inpainting.

We reaffirmed our observations above on image denoising and inpainting, as shown in Fig. 20, Fig. 22, Fig. 23 and Fig. 21.

We argue that the understanding of the upsampling and its interactions with other architectural elements can help explain why deeper networks with fewer skip connections converge more slowly, generate smoother outputs and are less prone to overfitting. Concretely, the upsampling operation inserted in-between the decoder layer **slows down the generation of high frequencies** required for transforming the lower-resolution feature maps into the higher-resolution target image, **primarily due to its role as a fixed low-pass filter**. As the network depth increases, the degree of smoothness increases (Fig. 22). Skip connections notably accelerate the convergence (Fig. 21) and ameliorate the over-smoothing issue, likely due to the reduced "effective" upsampling rate. All these observations are consistent with our MRI experiments in Sec. 7.

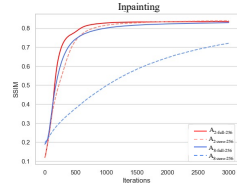


Fig. 21: Deep architectures with zero skip connection converge more slowly, i.e., $\mathbf{A}_{8\text{-zero-256}}$

E Comparisons with ZS-SSL-UNet

In the main paper, we have included the results of the ResNet version of ZS-SSL [48]. Here, we constructed a UNet variant of it, dubbed ZS-SSL-UNet. As shown in Tab. 8, the architecture type impacts not only DIP but also deep unrolling networks, and potentially a broader area, which worth future investigations.

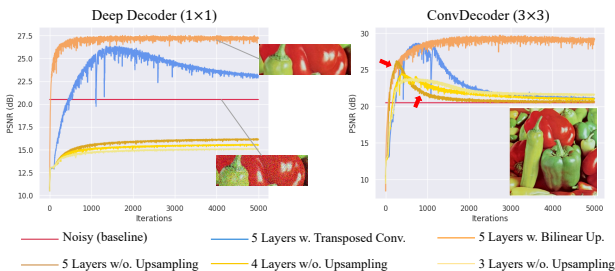


Fig. 20: Denoising experiments. (Left) In non-convolutional networks, **removing the upsampling hampers the denoising capability**, which cannot be compensated by merely adjusting the network to be more under-parameterized. Transposed convolutions result in a more rapid decline in performance than bilinear upsampling. (Right) Convolutional layers *alone* exhibit certain denoising effects but necessitate early stopping. The showcased image is from the classic dataset Set9 [8].

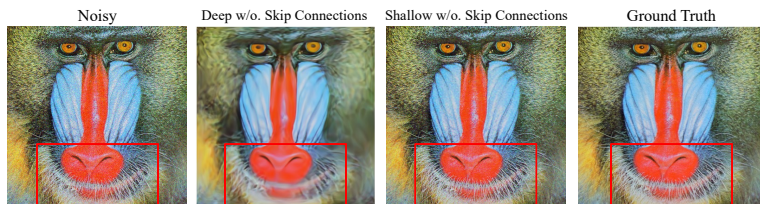


Fig. 22: Denoising experiments. Deeper architectures with few or no skip connections tend to generate smoother outputs compared to the shallower ones.

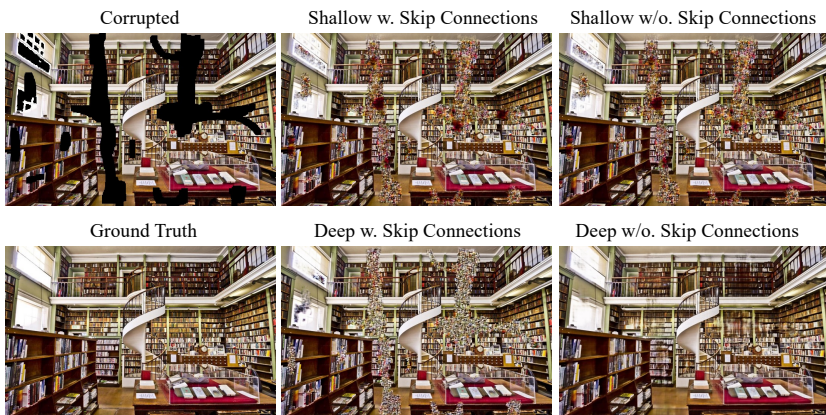


Fig. 23: Inpainting experiments. Deeper architectures with few or no skip connections tend to generate smoother predictions for the masked regions than the shallower architectures. Skip connections make deep architectures perform similarly as the shallower ones.

Table 8: Quantitative evaluations. Runtime: mean \pm std mins per slice.

	fastMRI Brain		fastMRI Knee		Stanford FSE		Runtime
	PSNR	SSIM	PSNR	SSIM	PSNR	SSIM	Avg
ZS-SSL-ResNet [48]	34.39	0.878	32.00	0.773	31.74	0.805	45.5 \pm 11.8 mins
ZS-SSL-UNet*	25.70	0.670	27.79	0.703	26.73	0.674	97.5 \pm 41.2 mins
Ours	33.10	0.874	32.07	0.781	31.30	0.800	4.4 \pm 0.4 mins